RSC Advances

ROYAL SOCIETY OF CHEMISTRY

www.rsc.org/advances

Cite this: DOI: 10.1039/c0xx00000x

www.rsc.org/xxxxxx

ARTICLE TYPE

Dramatic Activity of Bi_2WO_6@g-C_3N_4 Photocatalyst with Core@Shell Structure

Li Liu, Yuehong Qi, Jinrong Lu, Shuanglong Lin, Weijia An, Jinshan Hu*, Yinghua Liang, Wenquan Cui*

Received (in XXX, XXX) Xth XXXXXXXXX 20XX, Accepted Xth XXXXXXXXX 20XX
DOI: 10.1039/b000000x

Here we report a Bi_2WO_6@g-C_3N_4 core@shell structure which was prepared by a combined ultrasonication-chemisorption method with enhanced photocatalytic degradation. The composites were extensively characterized by X-ray diffraction (XRD), Fourier transform infrared spectra (FTIR), scanning electron microscopy (SEM), transmission electron microscopy (TEM) and UV-vis diffuse reflectance spectroscopy (DRS). Compared with bare Bi_2WO_6 and g-C_3N_4, the Bi_2WO_6@g-C_3N_4 composites exhibited significantly enhanced photocatalytic activity for methylene blue (MB) degradation under visible light irradiation. The 3 wt. % Bi_2WO_6@g-C_3N_4 showed the highest photocatalytic activity under visible light irradiation, which was about 1.97 times than Bi_2WO_6. In addition, the quenching effects of different scavengers displayed that the reactive h^+ and $\bullet O_2^-$ play the major role in the MB decolorization. The core@shell hybrid photocatalysts exhibited dramatically enhanced photo-induced electron-hole separation efficiency, which was confirmed by the results of photocurrent and EIS measurements. On the basis of the experimental results and estimated energy band positions, the mechanism of enhanced photocatalytic activity was proposed.

1. Introduction

Recently, the ever-growing emission of dye wastewater from various industries such as textiles, printing, food and cosmetics has become a major threat to human and ecology owing to the toxicity and non-biodegradability. Heterogeneous photocatalysis appears to be one of the most efficient and economic techniques for the remediation of a contaminated environment [1, 2]. However, traditional photocatalyst still cannot fully meet the requirement of practical application in environmental cleaning and hydrogen producting driven by solar energy due to wide band gap and rapid recombination of photo-generated electrons and holes [3, 4]. Up to now, the development of visible-light-driven semiconductor photocatalysts that can directly degrade organic compounds in water remains a great challenge.

Bismuth tungstate (Bi_2WO_6), with a narrow band gap of 2.8 eV, has been confirmed to present amusing solar or visible-light photocatalytic performance in water-splitting and organic pollutants degradation [5]. Various morphology and structure of Bi_2WO_6 photocatalysts have also been found to improve the photocatalytic activity [6-9]. Although the strategy of shape control can improve the photocatalytic performance of Bi_2WO_6, high recombination of photogenerated carriers between the hybrid orbital of Bi 6s and O 2p to the empty W 5d orbital results in low photo quantum efficiency of Bi_2WO_6[10-12]. Recent studies have shown that coupling of Bi_2WO_6 with other semiconductors improve the photocatalytic performance of Bi_2WO_6 to a substantial extent by promoting the effective separation of photoinduced charge carriers and broadening the visible light responsive range, such as BiOI[13], TiO_2[14], AgBr[15] and CdS[16]. These new composite photocatalysts greatly improved the practical application in the utilization of solar energy. However, the point contact caused by these bulk phase recombination could lead to low conjunction of Bi_2WO_6 with π-conjugated material, which could limit the photo-induced charge separation.

Photocatalysts with core@shell nanostructures possess excellent visible-light-driven photocatalytic activity and many advantages [17, 18]. Compared with point contact, the core@shell architecture maximizes interaction area between the core and the semiconductor shell, facilitates the separation of the photogenerated charge carriers[19]. Moreover, coupling with different semiconductor can introduce a strong interface electric field by band-edge offset, and accelerate the separation of photogenerated charge carriers. Recently, a polymeric photocatalyst made of graphitic carbon nitride (g-C_3N_4) has attracted much attention [20-23]. The well-crystallized g-C_3N_4 is a well-known π-conjugated material in the improvement of the photogenerated electron-hole pair separation. More importantly, the s-triazine ring structure and the high condensation of g-C_3N_4 make the polymer highly stable to temperature (up to 600°C in air) and chemical exposure (e.g., acid, base, and organic solvents) [24]. In addition, g-C_3N_4 is a soft polymer and it can be easily used for coating. Many materials have been coupled with g-C_3N_4 to inform the core@shell structure, such as CdS [25], Cu_2O [26], ZnO [27] or $BiPO_4$ [17]. And also, by comparing the energy levels of g-C_3N_4 with Bi_2WO_6, it is fortunate to find that the energy levels of g-C_3N_4 and Bi_2WO_6 are well-matched overlapping band-structures, favoring the charge transfer generated by semiconductors under light irradiation, prolonging the lifetime of electron-hole pairs.

In this study, we report the novel core@shell composites comprising of Bi_2WO_6 and g-C_3N_4. The photocatalytic activity of

as-obtained Bi_2WO_6@g-C_3N_4 nanocomposites has been investigated under artificial solar light irradiation by using several probe reactions, including the oxidative degradation of MB, RhB MO and phenol. The obtained composites show significantly enhanced photocatalytic activities for the degradation of organic compounds under visible light irradiation. According to optical and photoelectrical analysis, the reason is mainly attributed to the extended visible-light response and the prolonged lifetime of photogenerated carriers in Bi_2WO_6@g-C_3N_4 interfaces. In addition, the possible mechanism of Bi_2WO_6@g-C_3N_4 photocatalysis is discussed based on main oxidative species detection experiments, transient photocurrent and electrochemical impedance spectroscopy technique.

2. Experimental

2.1. Synthesis of photocatalysts

Synthesis of g-C_3N_4 and g-C_3N_4 nanosheets

All chemicals were reagent grade and used without further purification. Typically, 10 g of melamine was put into an alumina crucible with a cover and heated at a rate of 2°C min^{-1} to 550°C in a muffle furnace and then kept at this temperature for 4 h. All the experiments were performed under air conditions. The resulting yellow product was collected and ground into powder for further use. In brief, 0.05 g of g-C_3N_4 was ultrasonicated in 50 mL of water for 24 h and centrifuged at about 2000 rmp to remove the unexfoliated g-C_3N_4. Finally, the suspension of ultrathin g-C_3N_4 nanosheets was used for further study.

Synthesis of Bi_2WO_6

Bi_2WO_6 was prepared by a precipitation method. Briefly, 1.46 g amount of $Bi(NO_3)_3 \cdot 5H_2O$ and 0.50 g of $Na_2WO_4 \cdot 2H_2O$ were dissolved in 40 mL of ethylene alcohol separately under magnetic stirring at room temperature. After mixing the two solutions, a transparent mixture (80 mL) was obtained transferred into a 100 mL Teflon-lined autoclave and subsequently heated at 160°C for 13 h. The reactor was then allowed to cool to room temperature naturally. The precipitate was collected and washed with distilled water, and the final products dried at 60°C for 12 h.

Synthesis of Bi_2WO_6@g-C_3N_4

The concentration of ultra-thin g-C_3N_4 nanosheets suspension was estimated to be about 0.12 mg/mL. A certain amount of Bi_2WO_6 was added to the ultrathin g-C_3N_4 nanosheets dispersion (100 ml) and stirred for 48 h. The nominal weight ratios of g-C_3N_4 to Bi_2WO_6 were 1, 2, 3, 5 and 10 wt %, and weight of Bi_2WO_6 was 1.2 g, 0.6g, 0.4 g, 0.24g and 0.12 g, respectively. The water was evaporated and the residue was dried at 60 °C for 24 h to obtain a Bi_2WO_6@g-C_3N_4 composite powder.

2.2. Characterization of the photocatalysts

The crystal structures and phase states of Bi_2WO_6@g-C_3N_4 composites were determined by X-ray diffractometry (XRD) using a Rigaku D/MAX2500 PC diffractometer with Cu Kα radiation at an operating voltage of 40 kV and an operating current of 100 mA. The Fourier transform infrared spectra (FTIR) of the samples were recorded on an IR Vertex70 FTIR spectrometer. The morphologies of the samples were imaged with a scanning electron microscopy (SEM) (Hitachi, s-4800) and a transmission electron microscopy (TEM) (JEOL Ltd., JEM-2010). UV-visible light (UV-Vis) diffuse reflectance spectra were recorded on a UV-Vis spectrometer (Puxi, UV1901). Electrochemical and photoelectrochemical measurements were performed in 0.1 M Na_2SO_4 electrolyte solution in a three-electrode quartz cell. Pt sheet was used as a counter electrode and Hg/Hg_2Cl_2/sat. KCl was used as a reference electrode. The Bi_2WO_6@g-C_3N_4 composite thin film on indium-tin oxide (ITO) was used as the working electrode for investigation. The photoelectrochemical response was recorded with a CHI 660B electrochemical system.

2.3. Photocatalytic activity

The photocatalytic activities of Bi_2WO_6@g-C_3N_4 composites were evaluated with its catalytic degradation of MB under irradiation of visible light. A 250 W halide lamp (Philips) with a 420 nm cutoff filter was located at a distance of 10 cm from an unsealed beaker for the first test group. A glass reactor with 25±2 °C circulating water flowing outside was employed for the secondary test group. For each test, 0.25 g catalyst powder was added into 50 mL 10 mg/L MB solution. The test solutions were stirred in the dark for 30 min before irradiated under the visible light. During the irradiation, a 3 mL sample of the reaction suspension was taken every 5 minutes and centrifuged at 10000 rpm for 6min. The supernatant was collected and analyzed on the UV-vis spectrophotometer.

Photocatalytic degradations of MB in the dark in the presence of the photocatalyst and under visible-light irradiation in the absence of the photocatalyst were also used as negative controls. In addition, the degradation of RhB and MO was investigated with the same procedure.

3. Result and discussion

3.1. Characterization of catalysts

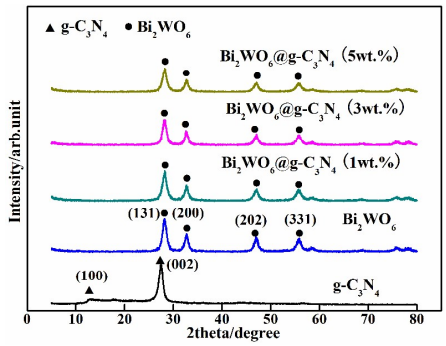

Fig.1 XRD patterns of g-C_3N_4, Bi_2WO_6, Bi_2WO_6@g-C_3N_4 photocatalysts.

The crystal structure of the product was characterized by X-ray diffraction (XRD). The typical XRD patterns of Bi_2WO_6 and Bi_2WO_6@g-C_3N_4 composite are shown in Fig. 1. Two characteristic peaks are observed for bulk g-C_3N_4. The peak observed at 13.1°corresponds to the in-plane structural packing motif of tristriazine units and is indexed as the (100) peak. Another intense peak at 27.5° corresponds to the interlayer stacking of aromatic segments with a distance of 0.324 nm, which is indexed as the (002) peak of the stacking of the conjugated aromatic system [28]. According to Fig. 1, the diffraction peaks at 28.3°, 32.8°, 47.1° and 55.8° corresponding to the (131), (200),

(202) and (331) crystallographic planes of orthorhombic Bi_2WO_6 [29]. Compared with diffraction pattern of bare Bi_2WO_6, no signicant diffraction peaks of any other phase or impurity was observed on Bi_2WO_6@g-C_3N_4 composites indicating that the characteristic peaks associated with g-C_3N_4 are not obviously detected, which due to the limit use of g-C_3N_4. Nevertheless, the presence of g-C_3N_4 could be confirmed by XPS analyses when its content was increased to 3 wt. %.

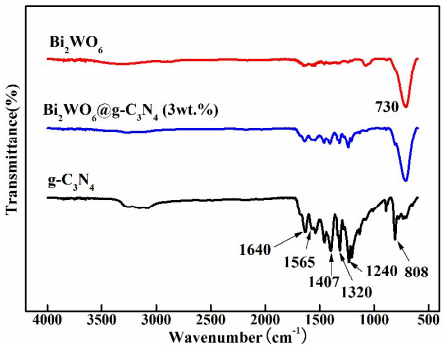

Fig. 2 FTIR spectra of the prepared g-C_3N_4, Bi_2WO_6 and Bi_2WO_6@g-C_3N_4 photocatalysts

The composition of Bi_2WO_6@g-C_3N_4 was further characterized by FTIR spectroscopy (Fig. 2). The characteristic absorption bands of Bi_2WO_6 appeared in 730 cm^{-1}, which corresponded to W-O stretching in the Bi_2WO_6 [30, 31]. No characteristic absorption peak of the ionic liquids is found in the FTIR spectra, it shows that the ionic liquid can be easily removed from the surface of the material by washing with deionized water and alcohol. For the pure g-C_3N_4, three main absorption regions can be observed clearly. The broad peak at 3000-3500 cm^{-1} is ascribed to the stretching vibration of N-H and the stretching vibration of O-H of the physically adsorbed water [32-34]. The strong bands between 1200-1700 cm^{-1}, with the characteristic peaks at 1240, 1320, 1407, 1567, and 1640 cm^{-1}, are attributed to the typical stretching vibration of CN heterocycles [32]. In addition, the peak at 808 cm^{-1} corresponds to the breathing mode of triazine units [32, 34]. The characteristic bands of Bi_2WO_6 still remained in the Bi_2WO_6@g-C_3N_4 composite, but the typical absorption peaks of g-C_3N_4 decreased dramatically in intensity or even disappeared as compared with those of pure g-C_3N_4, indicating the reduction of g-C_3N_4.

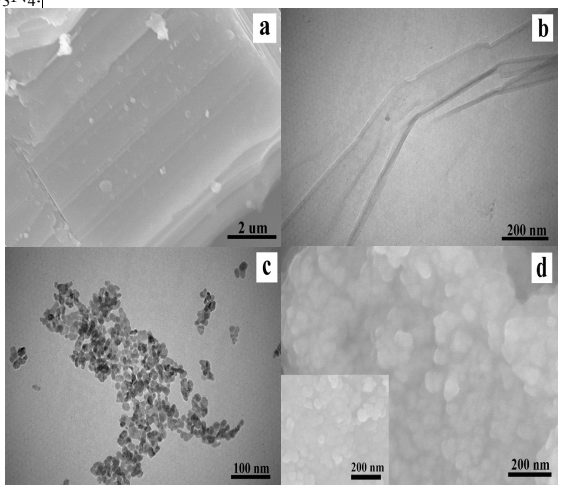

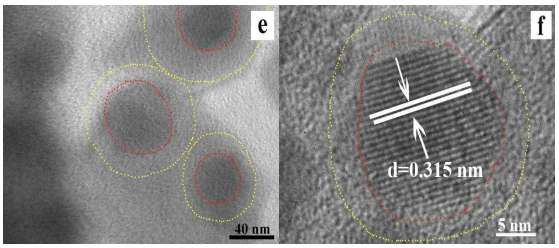

Fig. 3 SEM image of g-C_3N_4 (a), TEM images of g-C_3N_4 nanosheets (b) and Bi_2WO_6 (c), SEM (d) image of Bi_2WO_6@g-C_3N_4(inset in (d) SEM image of Bi_2WO_6), TEM (e) and HRTEM (f) images of Bi_2WO_6@g-C_3N_4.

The morphologies of the g-C_3N_4, Bi_2WO_6 and Bi_2WO_6@g-C_3N_4 (3wt. %) composite were revealed by SEM and TEM. Fig. 3a shows the SEM micrographs of pure g-C_3N_4 sample. Bluk g-C_3N_4 are solid agglomerates of several micrometers in size. Flakes with laminar morphology were observed of g-C_3N_4 nanosheets after ultrasonic exfoliation. The TEM image of the product after ultrasonic exfoliation as presented in Fig. 3b, which shows that the displayed layer possesses chiffon-like ripples and wrinkles. The morphology of g-C_3N_4 suggests that g-C_3N_4 nanosheets were successful obtained in the reaction of water solution. Ultrathin nanosheets maintain the stable suspension over a long time in water due to its matching surface energy with bulk g-C_3N_4 and its highest polarity among solvents [35]. In addition, the ultrathin nanosheets are so soft that in can easily coated the surface of Bi_2WO_6 nanospheres. Fig. 3c indicates that the sample of Bi_2WO_6 is shaped into uniform sphere morphology with average size of 30-40 nm. Fig. 3d shows the SEM images of the Bi_2WO_6@g-C_3N_4. Compared with Bi_2WO_6 nanospheres (inset in Fig. d), Bi_2WO_6@g-C_3N_4 could be obtained whose surface is distinctly enwrapped with gauze-like g-C_3N_4 nanosheets. However, the SEM images have not enough resolution for analysis of the core@shell structure. The morphological and structural features of samples were further examined by TEM/HRTEM. g-C_3N_4 was successfully coated over Bi_2WO_6 nanospheres with intimate contact in a spontaneous adsorption process, and the core@shell structures can be clearly observed in TEM image(Fig. 3e) due to the different electron penetrability between the cores and the shells. From the HRTEM image of Bi_2WO_6@g-C_3N_4 nanocomposite (Fig. 3f), the clear lattice fringes with a spacing of 0.315 nm can be assigned to (131) lattice planes of orthorhombic Bi_2WO_6, which is in good agreement with XRD results. The outer layer of the as-prepared Bi_2WO_6@g-C_3N_4 sample is distinctly different from the Bi_2WO_6 core. TEM image indicated that the exfoliated g-C_3N_4 sheets were preferentially coated on the lateral surface of the nanospheres to achieve a minimum surface energy. When the morphology of the pure Bi_2WO_6 is compared with that of Bi_2WO_6@g-C_3N_4, it is obvious the g-C_3N_4 sheets can coat with Bi_2WO_6 to prevent their aggregation. The homogeneous attachment of Bi_2WO_6 nanospheres with g-C_3N_4 sheets is beneficial for the separation of photogenerated charge, which can prolong the lifetime of electron-hole pairs. In order to measure the amount of g-C_3N_4 in the composite, X-ray fluorescence spectrometer (XRF) analysis

for the Bi_2WO_6@g-C_3N_4 (3wt.%) was performed. The elemental contents of C and N are found to be 1.02 wt.% and 1.78 wt.%, respectively, the calculated value of g-C_3N_4 content in the composite was about 3 (mass%).

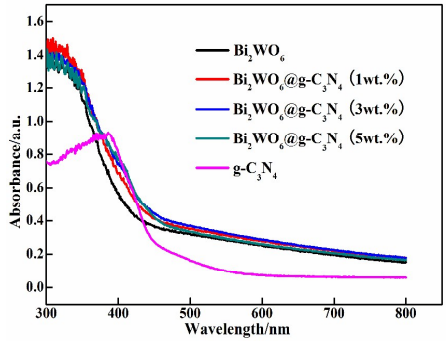

Fig.4 UV-vis diffuse reflectance spectra of prepared photocatalysts

Fig. 4 displays the UV-vis diffuse reflectance spectra of bare Bi_2WO_6 and Bi_2WO_6@g-C_3N_4 composite. The absorption edge of pure g-C_3N_4 photocatalysts is about 460 nm, with band gap (Eg) calculated to be 2.7 eV [36]. The absorption threshold of Bi_2WO_6 is located at around 450 nm due to the intrinsic band-gap transition corresponding to the Eg of 2.8 eV [5, 37]. Further Bi_2WO_6@g-C_3N_4 shows the broader absorption edge and extends to the visible region as compared to that of Bi_2WO_6 due to the presence of g-C_3N_4 on the Bi_2WO_6 surface. It is notable that compared with Bi_2WO_6 surface, the absorption edge of Bi_2WO_6@g-C_3N_4 experiences a red shift of about 10-20 nm. This observation was mainly attributed to the light shielding of Bi_2WO_6 covered by g-C_3N_4. The absorption intensity of the prepared composites varied with the content of g-C_3N_4.

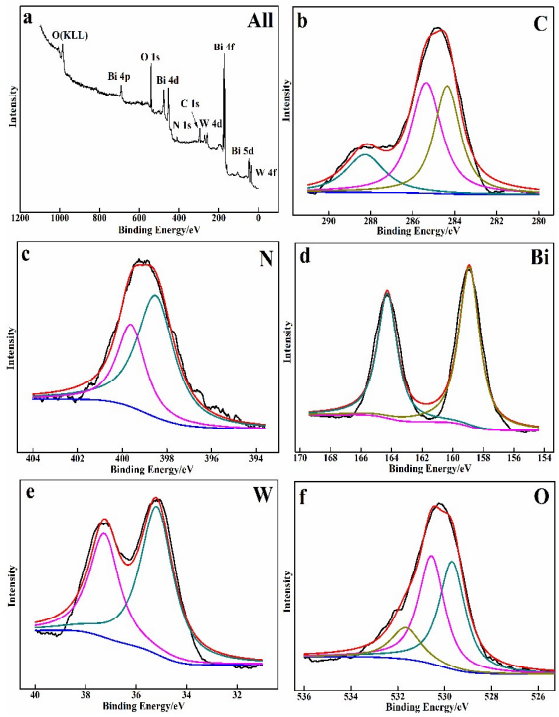

Fig.5 XPS spectra of (a) survey spectrum, (b) C, (c) N, (d) Bi, (e) W and (f) O of the sample 3 wt.% Bi_2WO_6@g-C_3N_4.

The surface elemental composites and chemical environment variation of samples were analyzed by XPS. Fig. 5a is XPS survey spectra of 3 wt.% Bi_2WO_6@g-C_3N_4. Typical survey XPS spectrum of Bi_2WO_6@g-C_3N_4 indicates that C, N, Bi, W and O elements could all be detected as shown in Fig. 5a. In Fig. 5b, the C 1s spectrum can be found in three peaks of 284.4, 285.4 and 288.2 eV. The peak at around 284.4 eV is regarded as graphitic carbon, whereas the peak at 285.4 eV is ascribed to C-NH_2 species on the g-C_3N_4 [27]. The peak at 288.2 eV corresponded to the sp^2-hybridized carbon in N-C=N coordination [38, 39]. XPS spectrum of N 1s can be deconvoluted into two peaks centered at 399.7 eV and 398.5 eV, respectively, corresponding to the nitrogen atoms in the aromatic rings (C-N=C) and tertiary nitrogen (N-$(C)_3$) [40, 41]. As shown in Fig. 5d, the peaks at 164.3 and 158.9 eV, corresponding to Bi $4f_{5/2}$ and Bi $4f_{7/2}$, can be assigned to Bi^{3+} of bare Bi_2WO_6 [42]. The peaks at 37.6 and 35.2 eV can be assigned to W $4f_{5/2}$ and W $4f_{7/2}$, respectively (Fig. 5e), which represent a W^{6+} oxidation state [43]. The O 1s spectrum could be fitted by three peaks at binding energies of 531.7, 530.6 and 529.7 eV respectively, which are shown in Fig. 5f. The peak at 531.7 and 529.8 eV are consistent with the different chemical environments of oxygen element in Bi-O and W-O. The peaks at 530.6 correspond to the hydroxyl groups on the surface of Bi_2WO_6 [44].

3.2. Photocatalytic activity

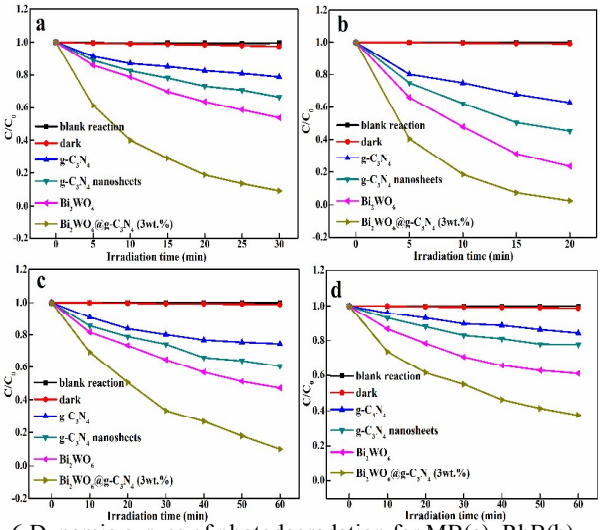

Fig. 6 Dynamic curves of photodegradation for MB(a), RhB(b) MO (c) and phenol (d) solutions over different samples.

The photocatalytic performance of the as synthesized Bi_2WO_6@g-C_3N_4 product was evaluated by degradation of MB under simulated sunlight irradiation. Fig. 6a displays the changes of the MB concentration versus the reaction time over the Bi_2WO_6@g-C_3N_4 photocatalysts. Simple photolysis of MB was also carried out for comparison. No MB was photodegraded by the visible light in the absence of photocatalyst, indicating that the contribution of photolysis of MB to the photoactivity was negligible. As shown in Fig. 6a, it is clear that the concentration of the MB solution gradually decreases during the photodegradation. Only 21.2% MB can be photodegraded by bulk g-C_3N_4 in 30 min. g-C_3N_4 nanosheets possess the bigger of BET

specific surface areas. In that case, the g-C_3N_4 nanosheets show improved photocatalytic activity and degrade nearly 33.6% of MB[45]. The use of Bi_2WO_6 leads to 46.2% photodegradation of MB. Nearly 90.8% of MB was degraded after 30 min irradiation in the presence of Bi_2WO_6@g-C_3N_4 photocatalyst, indicating its excellent photocatalystic activity. Besides the degradation of pollutant MB, the photocatalytic performance of Bi_2WO_6@g-C_3N_4 was further studied by degradation of pollutant RhB and MO. Similar to the photocatalytic degradation of MB, the Bi_2WO_6@g-C_3N_4 also exhibited evidently improved photocatalytic activity compared with the pure Bi_2WO_6 and g-C_3N_4 on the degradation of RhB and MB. Phenol is a colorless organic compound and was also chosen as a model contaminant. In the present work, the degradation of phenol over Bi_2WO_6@g-C_3N_4 under visible light irradiation (>420 nm) was also studied to further evaluate the photocatalytic performance of Bi_2WO_6@g-C_3N_4 composites. Under visible-light irradiation, the results of the photocatalytic evaluation of as-prepared samples are shown in in Fig. 6d. Phenol was degraded 39.1% over Bi_2WO_6 under visual light irradiation for 60 min. The degradation ratio was significantly increased to 62.6% over the Bi_2WO_6@g-C_3N_4 composite photocatalyst with a 60 min visible light irradiation. By comparison of the phenol degradation rates, the photocatalytic activity of Bi_2WO_6@g-C_3N_4 was confirmed for the degradation of phenol, and affirmed that the disappearance of phenol molecules was due to photocatalytic degradation instead of only to adsorption. Well-aligned band-structures and intimately contact interface enhance charge separation, which result in excellent photocatalytic activity.

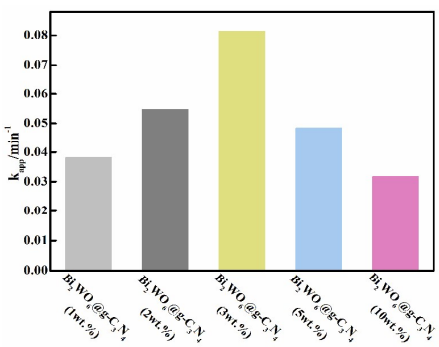

Fig. 7 Comparison of degradation of MB over Bi_2WO_6@g-C_3N_4 composite with various g-C_3N_4 contents of 1.0 wt.%, 2.0 wt.%, 3.0 wt.%, 5.0 wt.% and 10.0 wt.%.

g-C_3N_4 content has a significant influence on the photocatalytic activity of the composite. Photocatalytic degradation kinetic curve was investigated by the first-order simplification of Langmuir-Hinshelwood (L-H) kinetics, which is well established for photocatalysis at low initial pollutant concentrations. The relevant equation is as follows:

$$\mathrm{Ln}\,(C_0/C)=kt \qquad (1)$$

where C_0/C is the ratio of the concentration of the dyes at adsorption-desorption equilibrium and after various intervals of time, and k is the apparent first-order rate constant (min^{-1}). The value of k value is obtained from the gradient of the graph of ln(C_0/C) versus time (t), which is shown in the insert of Fig. 7. Obviously, the reaction rates constant k of Bi_2WO_6@g-C_3N_4 composites containing 1 wt. %, 2 wt. %, 3 wt. %, 5 wt. % and 10wt. % g-C_3N_4 were 0.03816, 0.05469, 0.08143, 0.04838 and 0.03174 min^{-1}, respectively. The photocatalytic activity of the Bi_2WO_6@g-C_3N_4 composites increased with the increase of g-C_3N_4 content from 1 to 3wt. %. When the g-C_3N_4 content was relatively low (<3.0 wt. %), the contact area gradually increased with the increment of g-C_3N_4. In this case, an effective charge separation can be achieved, resulting in enhancement of photocatalytic activity and inhibition of photocorrosion. At g-C_3N_4 content higher than the optimized content, excessive g-C_3N_4 covered on the surface of Bi_2WO_6 could form a dense shell. The dense shell suppress the electrons on the VB of Bi_2WO_6 transfer to surface of g-C_3N_4 and reduces the number of superoxide radicals which can act a main reactive species in the photocatalytic degradation. At the same time, this can facilitate the recombination of photoinduced electron-hole pairs. Consequently, the photocatalytic activity will decrease rapidly with further increasing of the g-C_3N_4 content. Therefore, it is important to make a balance between the active trapping sites favoring the inhibition of the recombination of electron-hole pairs and fewer trapped parts leading to a lower capacity for the separation of interfacial charge transfer.

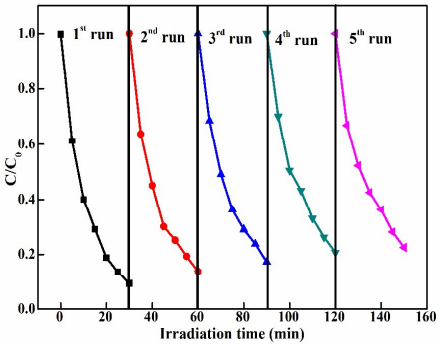

Fig. 8 Recycling runs of the degradation of MB over Bi_2WO_6@g-C_3N_4 (3wt.%) composite under visible-light irradiation (λ> 420 nm).

To evaluate the stability and reusability of the Bi_2WO_6@g-C_3N_4 hybrid photocatalyst, we carried out the additional experiments to degrade MB under visible light cycled forfive times (Fig. 8). After every run of photocatalytic reaction, the concentrated MB solution was injected and the separated photocatalysts were washed back into the reactor in order to keep the initial concentration of MB and photocatalysts constant. The recycling runs of the photocatalytic degradation of MB by the Bi_2WO_6@g-C_3N_4 (3wt. %) sample under visible-light were studied (Fig. 8). As shown in Fig. 10, the photocatalytic activity of Bi_2WO_6@g-C_3N_4 for MB degradation is effectively maintained from 90.8% to 77.5% after five cycling runs, which indicates that Bi_2WO_6@g-C_3N_4 has high stability in the photodegradation process under visible light. This decrease was thought to be due to some catalyst washout during the recovery steps, which could be minimized through the use of centrifugation between runs. Therefore, the results obtained illustrate that the incorporation of g-C_3N_4 into the Bi_2WO_6 matrix not only enhances the visible light photocatalytic performance of Bi_2WO_6, but also inhibits the photo-corrosion, thus giving rise to a stable durability of photocatalytic activity.

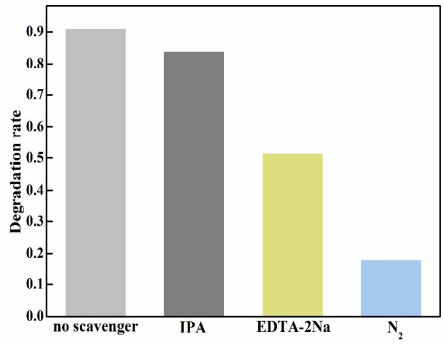

Fig. 9 Phaotocatalytic degradation of MB over Bi_2WO_6@g-C_3N_4 (3wt.%) in the presence of IPA, EDTA-2Na, N_2 and in the absence scavengers.

The electrons and holes produced by photocatalysis have strong reduction and oxidation abilities. However, they usually do not react with the organic dyes directly. Instead, some active species (such as •OH and •O_2^-) are first formed through the reaction of charges and adsorbed H_2O or O_2. So, it is important to detect main oxidative species in the photocatalytic process for elucidating the photocatalytic mechanism. The main oxidative species in photocatalytic process are detected through the trapping experiments of radicals using IPA as hydroxyl radical scavenger and EDTA-2Na as holes radical scavenger, and purging N_2 as •O_2^- scavenger, respectively [46]. If the free radical scavenged played acted an important role in the photocatalytic degradation of MB, the degradation rate would be reduced greatly in the presence of the appropriate scavenger. Before irradiation, the scavenger (10 mmol/L) was added to the MB solutions together with the catalyst. As is clear from Fig. 9, the addition of IPA did not affect the decolorization rate of MB over Bi_2WO_6@g-C_3N_4 (3wt. %), suggesting that •OH was not main reactive species in the photocatalytic process. To further prove the existence of ·O_2^-, a control experiment was carried out under N_2 atmosphere, where N_2 was purged through the solution to remove the dissolved O_2 in water in order to reduce radicals. And as showed in Fig. 9, the degradation rate decreases obviously to 17.8% in the presence of N_2 (·O_2^- scavenger) and the degradation rate was 90.8% in the absence of scavengers, which suggests that •O_2^- is the main reactive species for MB degradation. Meanwhile, EDTA-2Na had a significant effect on the degradation rate compared to the runs performed in the absence of scavenger, suggesting that h^+ was also a dominant reactive species.

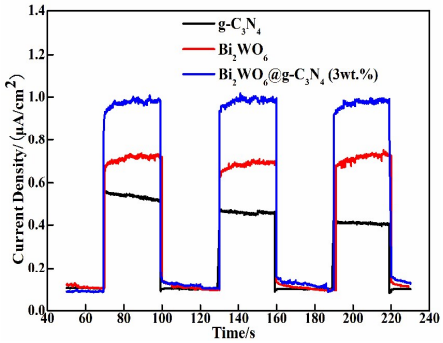

Fig. 10 Transient photocurrent of g-C_3N_4, Bi_2WO_6 and Bi_2WO_6@g-C_3N_4 under visible light irradiation.

It is well-known that the photocatalytic redox reactions are intimately relevant to the separation efficiencies of photoinduced electron-hole pairs arisen from the excited semiconductor materials [47]. Photocurrent can be produced from the photo-generated electrons in the conducting bands of semiconductor photocatalysts with leaving holes in their valence bands. Therefore, higher photocurrents are indicative of better electron and hole separation efficiencies, and thus higher photocatalytic activities [48]. Fig. 10 shows the current-voltage curves for these three samples under several on/off visible-light irradiation cycles. It is clear that uniform and reversible photocurrent responses are observed in all electrodes, indicating effective charge transfer and successful electron collection for these three samples within the photoelectrochemical cell. Experimental results reveal that Bi_2WO_6@g-C_3N_4 exhibit higher current density than the single-component semiconductors, which demonstrate that a more effective separation of photogenerated electron-hole pairs and faster interfacial charge transfer occur in the core@shell structure of Bi_2WO_6@g-C_3N_4.

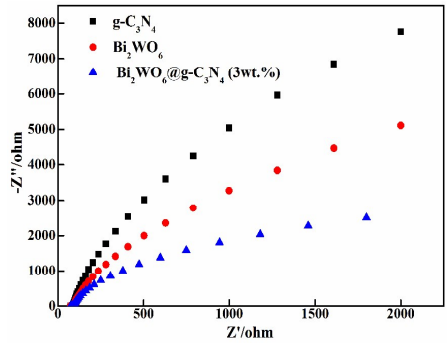

Fig. 11 Electrochemical impedance spectroscopy of g-C_3N_4, Bi_2WO_6 and Bi_2WO_6@g-C_3N_4.

As a powerful tool to explore the electrochemical process, EIS has been widely employed in testing the electro-catalytic activity for the regeneration of a redox couple [39, 49]. Fig. 11 reveals that the Nyquist plots diameter of 3 wt % Bi_2WO_6@g-C_3N_4 composite is much smaller over pristine Bi_2WO_6 and g-C_3N_4, suggesting the lower resistance and the faster interfacial charge transfer. This is consistent with the photocurrent results. This result demonstrates that the introduction of g-C_3N_4 into Bi_2WO_6 can enhance the separation and transfer efficiency of photogenerated electron-hole pairs, which is favorable for enhancing photocatalytic activity.

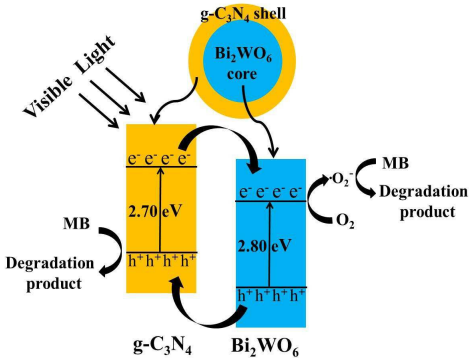

Fig. 12 Schematic illustration of the mechanism for the high photocatalytic performance of Bi_2WO_6@g-C_3N_4 composite

To approach the mechanism of the enhanced photocatalytic activity of the Bi_2WO_6@g-C_3N_4 composite, the relative band positions of the two semiconductors were investigated, since the band-edge potential levels play a crucial role in determining the flowchart of photoexcited charge carriers in the composite. As shown in the Fig. 12, the conduction band (CB) and valence band (VB) potentials of g-C_3N_4 (-1.3 and 1.4 eV) are more negative than those of Bi_2WO_6 (0.46 and 3.26 eV), suggesting that g-C_3N_4 and Bi_2WO_6 match the band potentials in the Bi_2WO_6@g-C_3N_4 composite [36, 50]. Under visible-light irradiation, both g-C_3N_4 and Bi_2WO_6 can absorb visible-light photons to produce photo-generated electrons and holes. The electrons were promoted from the VB to the CB of g-C_3N_4 and Bi_2WO_6, leaving the holes behind. Obviously, the difference between the CB edge potentials of g-C_3N_4 and Bi_2WO_6 allowed the electron transfer from the CB of g-C_3N_4 to that of Bi_2WO_6. Subsequently, simultaneous holes on the VB of Bi_2WO_6 migrated to that of g-C_3N_4 because of the enjoined electric fields of the two materials. In such a way, the photogenerated electrons can be effectively collected by Bi_2WO_6 and holes can be effectively collected by g-C_3N_4. Therefore, the efficiently separation of photogenerated electrons and holes can be achieved, and the recombination process of electron-hole pairs can be hindered, in accordance with the result of photocurrent and EIS. The electrons in Bi_2WO_6 crystals are good reductants that could capture the adsorbed O_2 onto the composite catalyst surface and reduce it to $\bullet O_2^-$. The highly oxidative species •OH is produced as a consequence of the reduction of oxygen. Under the action of substantial strong oxidizing species, the structure of MB was destroyed and finally decomposed into degradation products.

4. Conclusions

In summary, g-C_3N_4 can be successfully coated onto the surface of Bi_2WO_6 and a series of Bi_2WO_6@g-C_3N_4 photocatalysts with different varying compositions of g-C_3N_4 and Bi_2WO_6 were prepared. The g-C_3N_4 coated Bi_2WO_6 exhibits enhanced photocatalytic activity in the degradation of MB under visible light irradiation, which is higher than that of pure Bi_2WO_6, and the content of g-C_3N_4 impacts the catalytic activity of Bi_2WO_6@g-C_3N_4. The photocatalytic activity of as-prepared 3.0wt.% Bi_2WO_6@g-C_3N_4 exhibited the best photocatalytic activity. The mechanism has been discussed by energy band positions and photocurrent and EIS measurements. The enhanced photocatalytic activity can be attributed to the efficient separation and recombination preventing of electron-hole pairs. Both $\bullet O_2^-$ and photogenerated holes are the main reactive species responsible for the degradation of MB. Furthermore, Bi_2WO_6@g-C_3N_4 has high stability and are easily recyclable, suggesting that the photocatalyst is a promising photocatalytic material which has good potential for application to pollutants purification.

Acknowledgements

This work was financially supported by the National Natural Science Foundation of China (No. 51372068), Hebei Natural Science Funds for Distinguished Young Scholar (No. B2014209304), Hebei Natural Science Funds for the Joint Research of Iron and Steel (grant No. B2014209314).

Notes and references

College of Chemical Engineering, North China University of Science and Technology, Tangshan, 063009, P. R, China. Tel.: +86 315 2592169; E-mail: wkcui@163.com (W. Cui) and hu_jinshan@163.com (J. Hu).

1. Hoffmann M R, Martin S T, Chio W *et al*. *Chemical Reviews*[J]. 1995, 95, 69-96.
2. Chong M N, Jin B, Chow C W K *et al*. *Water Research*[J]. 2010, 44, 2997-3027.
3. Zhu J, Ren J, Huo Y N *et al*. *The Journal of Physical Chemistry C*[J]. 2007, 111, 18965-18969.
4. Li P, Wei Z, Wu T *et al*. *Journal of the American Chemical Society*[J] 2011, 133, 5660-5663.
5. Tian Y L, Chang B B, Lu J L *et al*. *ACS Applied Materials & Interfaces*[J]. 2013, 5, 7079-7085.
6. Zhao G, Liu S W, Lu Q F *et al*. *Industrial & Engineering Chemistry Research*[J]. 2012, 51, 10307-10312.
7. Wu J, Duan F, Zheng Y *et al*. *The Journal of Physical Chemistry C*[J]. 2007, 111, 12866-12871.
8. Ma D K, Huang S M, Chen W X *et al*. *The Journal of Physical Chemistry C*[J]. 2009, 113, 4369-4374.
9. Shang M, Wang W Z, Xu H L *et al*. *Crystal Growth & Design*[J]. 2009, 9, 991-996.
10. Shamaila S, Sajjad A K L, Chen F *et al*. *Applied Catalysis B: Environmental*[J]. 2010, 94, 272-280.
11. Ren J, Wang W Z, Sun S M *et al*. *Applied Catalysis B: Environmental*[J]. 2009, 92, 50-55.
12. Guo Y D, Zhang G K, Liu J *et al*. *RSC Advances*[J]. 2013, 3, 2963-2970.
13. Chen Y F, Fang J Z, Lu S Y *et al*. *Journal of Chemical Technology and Biotechnology*[J]. 2015, 90, 947-954.
14. Shang M, Wang W Z, Zhang L *et al*. *The Journal of Physical Chemistry C*[J]. 2009, 113, 14727-14731.
15. Wang D J, Guo L, Zhen Y Z *et al*. *Journal of Materials Chemistry A*[J]. 2014, 2, 11716-11727.
16. Ge L, Liu J. *Applied Catalysis B: Environmental*[J]. 2011, 105, 289-297.
17. Pan C S, Xu J, Wang Y J *et al*. *Advanced Functional Materials*[J]. 2012, 22, 1518-1524.
18. Khanchandani S, Kundu S, Patra A *et al*. *The Journal of Physical Chemistry C*[J]. 2012, 116, 23653-23662.
19. Li Y G, Wei X L, Li H J *et al*. *RSC Advance*[J]. 2015, 5, 14074-14080.
20. Wang X C, Maeda K, Thomas A *et al*. *Nature Materials*[J]. 2009, 8, 76-80.
21. Cao S W, Low J X, Yu J G *et al*. *Advanced Materials*[J]. 2015, 27, 2150-2176.
22. Zhao Z W, Sun Y J, Dong F *et al*. *Nanoscale*[J]. 2015, 7, 15-37.
23. Cao S W, Yu J G. *The Journal of Physical Chemistry Letters*[J]. 2014, 5, 2101-2107.
24. Wang Y, Wang X C, Antonietti M. *Angewandte Chemie International Edition*[J]. 2012, 51, 68-89.
25. Zhang J Y, Wang Y H, Jin J *et al*. *ACS Applied Materials & Interfaces*[J]. 2013, 5, 10317-10324.
26. Liu L, Qi Y H, Hu J S *et al*. *Materials Letters*[J]. 2015, 158, 278-281.

27. Kumar S, Baruah A, Tonda S *et al*. *Nanoscale*[J]. 2014, 6, 4830-4842.
28. Liao G Z, Chen S, Quan X *et al*. *Journal of Materials Chemistry*[J]. 2012, 22, 2721 -2726.
29. Mehraj O, Pirzada B M, Mir N A *et al*. *RSC Advances*[J]. 2015, 5, 42910-42921.
30. Xia J X, Di J, Yin S *et al*. *RSC Advances*[J]. 2014, 4, 82-90.
31. Qamar M, Elsayed R B, Alhooshani K R *et al*. *ACS Applied Materials & Interfaces*[J]. 2015, 7, 1257-1269.
32. Yan S C, Li Z S, Zou Z G. *Langmuir*[J]. 2009, 25, 10397-10401.
33. Fu J, Tian Y L, Chang B B *et al*. *Journal of Materials Chemistry*[J]. 2012, 22, 21159-21166.
34. Bojdys M J, Muller J O, Antonietti M *et al*. *Chemistry-A European Journal*[J]. 2008, 14, 8177-8182.
35. Zhang X D, Xie X, Wang H *et al*. *Journal of the American Chemical Society*[J]. 2013, 135, 18-21.
36. Shi L, Liang L, Ma J *et al*. *Catalysis Science & Technology*[J]. 2014, 4, 758-765.
37. Liu C M, Liu J W, Zhang G Y *et al*. *RSC Advances*[J]. 2015, 5, 32333-32342.
38. Yin L S, Yuan Y P, Cao S W *et al*. *RSC Advances*[J]. 2014, 4, 6127-6132.
39. He F, Chen G, Yu Y G *et al*. *ACS Applied Materials & Interfaces*[J]. 2014, 6, 7171-7179.
40. Yin L S, Yuan Y P, Cao S W *et al*. *RSC Advances*[J]. 2014, 4, 6127-6132.
41. Cao S W, Yuan Y P, Fang J *et al*. *International Journal of Hydrogen Energy*[J]. 2013, 38, 1258-1266.
42. Yang J, Wang X H, Zhao X L *et al*. *The Journal of Physical Chemistry C*[J]. 2015, 119, 3068-3078.
43. Mao C C, Li M L, Fang Z G *et al*. *RSC Advances*[J]. 2013, 3, 6631-6639.
44. Yue L F, Wang S F, Shan G Q *et al*. *Applied Catalysis B: Environmental*[J]. 2015, 176-177, 11-19.
45. Zhu K X, Wang W J, Meng A *et al*. *RSC Advances*[J]. 2015, 5, 56239-56243.
46. Wu S Z, Li K, Zhang W. D. *Applied Surface Science*[J]. 2015, 324, 324-331.
47. Zhu Y P, Li M, Liu Y L *et al*. *The Journal of Physical Chemistry C*[J]. 2014, 118, 10963-10971.
48. Xiang Q J, Yu J G, Jaroniec M. *The Journal of Physical Chemistry C*[J]. 2011, 115, 7355-7363.
49. Huang L Y, Xu H, Li Y P *et al*. *Dalton Transactions*[J]. 2013, 42, 8606-8616.
50. Zhang Z J, Wang W Z, Wang L *et al*. *ACS Applied Materials & Interfaces*[J]. 2012, 4, 593-597.

Dramatic Activity of Bi_2WO_6@g-C_3N_4 Photocatalyst with Core@Shell Structure

Li Liu, Yuehong Qi, Jinrong Lu, Shuanglong Lin, Weijia An, Jinshan Hu Yinghua Liang, Wenquan Cui*

College of Chemical Engineering, North China University of Science and Technology, Hebei Provincial Key Laboratory of Inorganic Nonmetallic Materials, Tangshan, PR China, 063009

Corresponding author: Wenquan Cui, Email: wkcui@163.com, Tel: +86 315 2592169

Graphical abstract: